

# Coherent single-spin control with high-fidelity singlet-triplet readout in silicon

R. Zhao,<sup>1</sup> T. Tanttu,<sup>1</sup> K. Y. Tan,<sup>2</sup> B. Hensen,<sup>1</sup> K. W. Chan,<sup>1,\*</sup> J. C. C. Hwang,<sup>1,†</sup> R. C. C. Leon,<sup>1</sup>  
C. H. Yang,<sup>1</sup> W. Gilbert,<sup>1</sup> F. E. Hudson,<sup>1</sup> K. M. Itoh,<sup>3</sup> A. Morello,<sup>1</sup> A. Laucht,<sup>1</sup> and A. S. Dzurak<sup>1</sup>

<sup>1</sup>*Centre for Quantum Computation & Communication Technology,  
School of Electrical Engineering & Telecommunications,*

*University of New South Wales, Sydney, New South Wales 2052, Australia*

<sup>2</sup>*QCD Labs, COMP Centre of Excellence, Department of Applied Physics, Aalto University, 00076 AALTO, Finland*

<sup>3</sup>*School of Fundamental Science and Technology, Keio University,  
3-14-1 Hiyoshi, Kohoku-ku, Yokohama 223-8522, Japan*

(Dated: December 15, 2024)

Single electron spins in silicon can be used to realize quantum bits (qubits) that profit from the long coherence times inherent to the host material. When confined in quantum dots (QDs) under electrostatic gates in a silicon metal-oxide-semiconductor (Si-MOS) architecture, there is the added promise of scalability provided by the well-established industrial semiconductor manufacturing technology. However, most Si-MOS spin qubits produced to date employ quantum state readout via spin-dependent-tunnelling to an electron reservoir. This requires significant on-chip real estate, making it difficult to be implemented in large scale multi-qubit devices. Here, we address this challenge by combining coherent spin control with high-fidelity, single-shot, singlet-triplet readout. We employ Pauli-spin blockade in a double QD as a readout tool to achieve a fidelity of 99.3 %. This readout scheme allows us to implement coherent electron spin resonance (ESR) control at magnetic fields as low as 150 mT, corresponding to a carrier frequency of 4.2 GHz, eliminating the need for high-frequency microwave sources. We discover that the qubits decohere faster at low magnetic fields with  $T_2^{\text{Rabi}} = 18.6 \mu\text{s}$  and  $T_2^* = 1.4 \mu\text{s}$  at 150 mT. Their coherence is limited by spin flips of residual <sup>29</sup>Si nuclei in the isotopically enriched <sup>28</sup>Si host material (800 ppm <sup>29</sup>Si), that occur more frequently at lower fields. This finding highlights the importance of further isotopic enrichment of silicon substrates for the realization of a scalable quantum processor using Si-MOS technology.

The rapid progress of spin qubits in silicon QDs has been fuelled by coherent electron spin resonance (ESR), either driven by an ac magnetic- [1] or electric-field [2, 3]. To date, ESR has enabled the demonstration of high-fidelity single- and two-qubit logic gates approaching the fault tolerance threshold [4–9]. In most of these demonstrations, single-shot spin readout was performed via spin-selective tunnelling of a single spin to a reservoir [10], however this technique is problematic for the operation of large-scale multi-qubit architectures [11, 12]. In order to work, it would require complex, coherent single-spin shuttling [13, 14] or a chain of swap gate operations [15] to readout qubits distant from a reservoir. Furthermore, quantum error correction protocols require simultaneous spin-state readout at arbitrary locations in the large-scale qubit array [12]. The preferred method for spin-readout is, therefore, singlet-triplet (ST) readout via Pauli-spin blockade (PSB) in a double QD system [16]. Besides alleviating the design constraints imposed by reservoir readout, single-shot dispersive ST readout may leverage state-of-the-art reflectometry technology to enable gate-based sensors with extremely small on-chip footprint [17–19]. Furthermore, ST readout forms the foundation of parity measurements, a main ingredient of some quantum error correction protocols [12], and does

not require the Zeeman splitting energy to be much larger than the thermal broadening of the reservoir. It therefore constitutes a robust readout technique that allows qubit operation over a wide range of magnetic fields. Especially the low magnetic field regime is of interest as it results in a lower spin resonance frequency, simplifying microwave engineering and requiring less expensive signal generators. Overall, both coherent ESR and high-fidelity ST readout are identified as the key elements for the implementation of a scalable, Si-MOS based quantum processor [11, 12]. Previous demonstrations have shown the compatibility of these two techniques for electrons in GaAs [20, 21], holes in Si-MOS [22] and incoherently for electrons in Si-MOS [15].

In this work, we achieve coherent, single-electron spin control with high-fidelity ST readout at a dc magnetic field of 150 mT. The device consists of a linear array of Si-MOS QDs, electrostatically defined by a palladium (Pd) gate stack [23] on an isotopically enriched <sup>28</sup>Si epilayer [24] (see Methods section). Fig. 1(a) shows a false-coloured scanning electron micrograph of a device nominally identical to the one used in this study. A cross-sectional schematic is plotted in Fig. 1(b). We have labelled the QD accumulation gates (G1-G6), the confinement gate (CB) that confines the QDs laterally, the reservoir gate (RG) that accumulates the electron reservoir for loading and unloading electrons, the single-electron transistor (SET) charge sensor (ST, SLB, SRB), and the short of the broadband ESR antenna to apply MW pulses [25] for spin control.

\* Present address: Microsoft Quantum, Sydney.

† Present address: Research and Prototype Foundry, The University of Sydney.

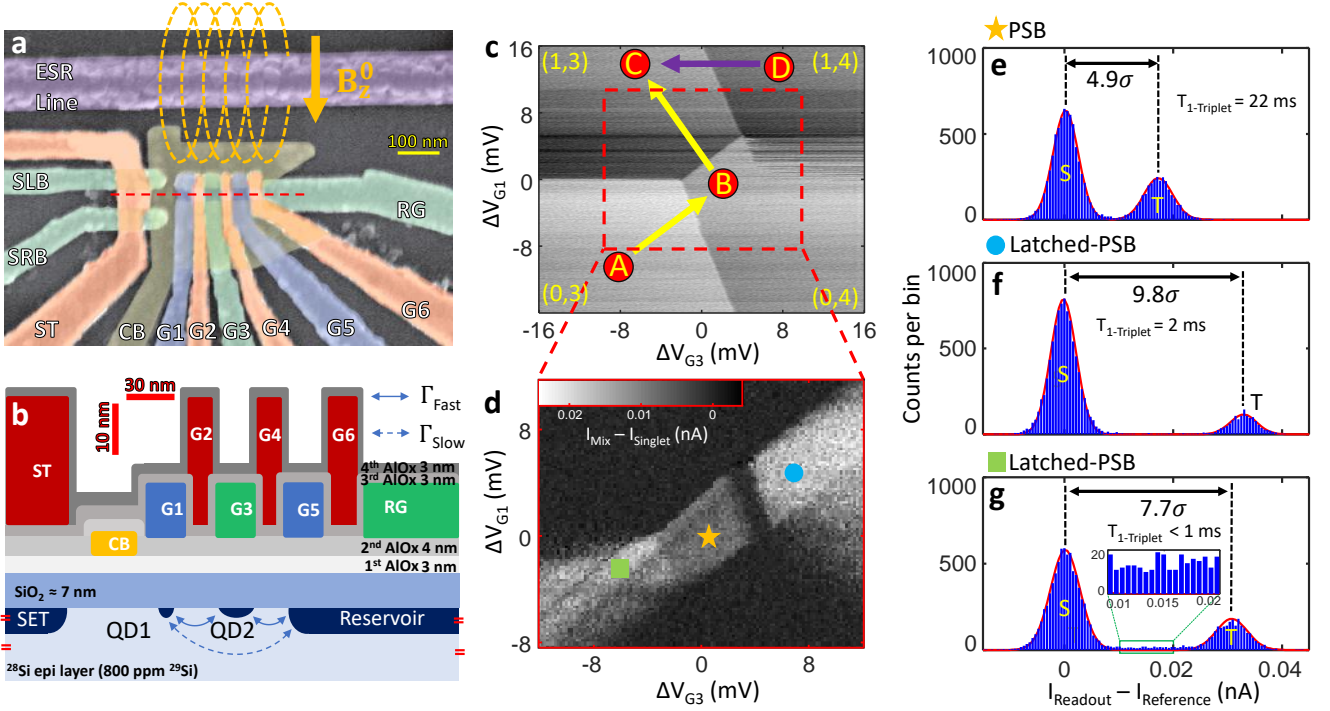


**Figure 1** | Device layout and high-fidelity singlet-triplet readout. (a), False-coloured scanning electron micrograph of a similar device. The orange arrow indicates the direction of the dc magnetic field  $B_z^0$ , which is aligned in plane to minimize spin-orbit coupling and reduce the qubits' sensitivity to charge noise. (b), Cross-sectional schematic along the red dashed line in (a), showing the Pd gate stack with insulating atomic-layer-deposited aluminium oxide layers. (c), Charge stability map around the (1,3) - (0,4) anti-crossing. The pulse sequence A-B-C (yellow arrows) prepares a separated double dot with electrons in the singlet state, while the pulse sequence D-C (blue arrow) prepares the double dot in a mixed state. The pulse sequence C-B facilitates the spin readout operation by attempting to push the electron from QD1 into QD2. Tunnelling will occur if the electron in QD1 forms a singlet with the electron in QD2, but it is blocked if the electrons form a triplet. (d), Difference in SET current between singlet and mixed spin state preparation, plotted as a function of the two gate voltages  $\Delta V_{G1}$  and  $\Delta V_{G3}$ . Apparent are the regions of standard PSB (star) and enhanced latching readout (circle, square). (e)-(g), Histograms of the SET current signal for 10200 single-shot readouts with 120  $\mu$ s integration time and 5 pA bin width, using the (e), standard PSB, or (f),(g), enhanced latching readout regions as indicated by the coloured markers in (d).

When tuning up the device, we use the following procedure to find the PSB region that gives us high-fidelity, single-shot ST readout. First, we carefully tune all the gate voltages to accumulate two QDs at the approximate locations indicated in Fig. 1(b), using the charge sensing technique described in Ref. 26. We then choose the (1,3) - (0,4) anti-crossing, shown in Fig. 1(c), as our working point. We assume the first two electrons in QD2 to form a singlet and not to interact with the third and fourth electrons during the experiment. Second, we either initialize the two QDs in a singlet state or in a mixed state of singlet and triplet. When pulsing from point A to point B (yellow arrow) we load a fourth electron on QD2, with the last two electrons forming an anti-parallel spin pair (singlet). Further pulsing to point C will separate these two electrons across the two QDs, keeping them in the singlet state. Alternatively, when pulsing from point D to C, we will randomly remove one of the four electrons from QD2. The spin of the remaining, third electron could be

either anti-parallel or parallel with the spin in QD1, leaving the two QDs initialized in a mix of triplet and singlet. Third, we find the region of PSB, by alternately initializing a singlet and a mixed state, and pulsing to a point around the (1,3) - (0,4) anti-crossing. Fig. 1(d) plots the difference in the SET current for the two different initializations, performed interleaved to reject slow drifts of the charge sensor. When the two QDs are in the singlet state, the single electron in QD1 can tunnel onto QD2 causing a change in charge configuration from (1,3) to (0,4). However, when they are in the triplet state, tunnelling is inhibited by PSB and the system remains in the (1,3) charge configuration [16]. Therefore, initialization into the mixed state will result in some probability for the charge sensor giving a reading that represents a triplet. We detect a clear standard PSB region and two enhanced latching regions, in which the highly-different tunnelling times from the QDs to the reservoir are used to cause a state dependent change in total charge [27].

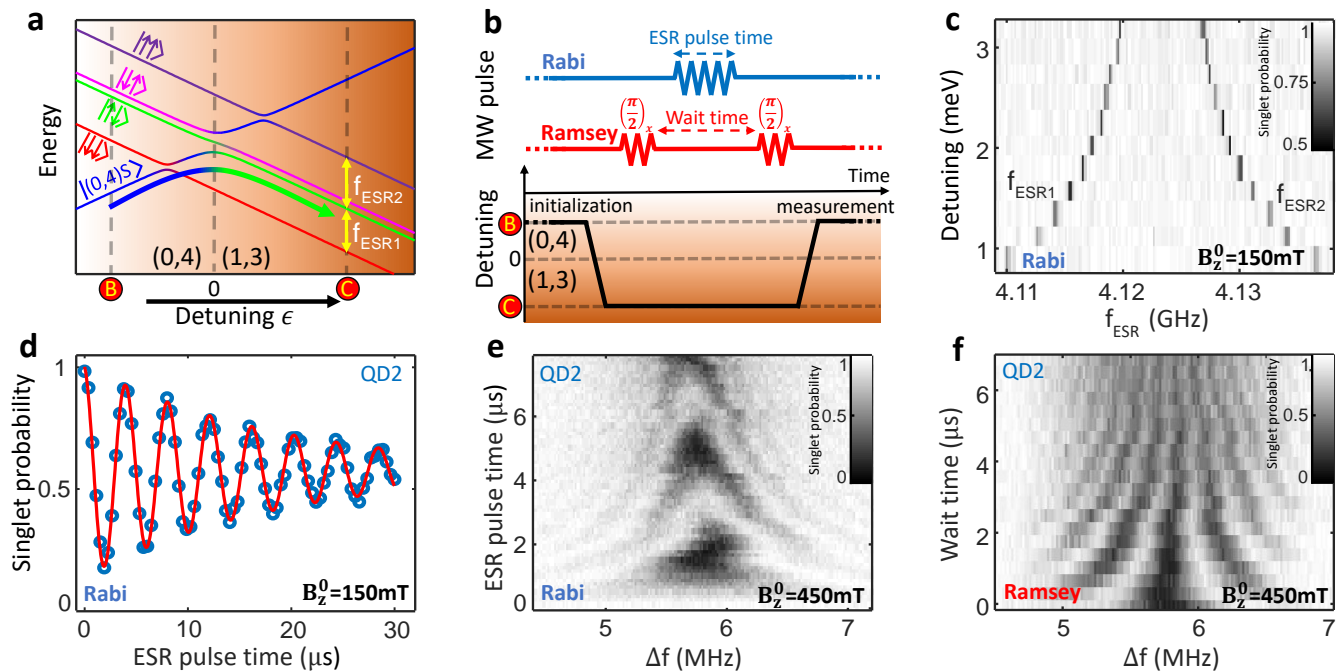


**Figure 2** | Coherent single-spin control with ST readout. (a) Schematic energy level diagram of the (1,3) - (0,4) anti-crossing. (b) Partial pulse sequences for the coherent spin control experiments in (d)-(f). The sequences start with initializing the system in the (0,4)S state by pulsing from point A to point B (see Fig. 1(c)). Then we prepare a  $|\uparrow\downarrow\rangle$  by moving from point B to point C. As indicated by the curved colour-graded arrow, we pulse diabatically across the S-T<sup>-</sup> anti-crossing, but adiabatically with respect to all the other anti-crossings. We then apply the microwave control pulses at the deep detuning point C to manipulate the individual spins. After spin manipulation, we perform readout by converting  $|\uparrow\downarrow\rangle$  back into singlet and  $|\uparrow\uparrow\rangle$  and  $|\downarrow\downarrow\rangle$  into triplet, by pulsing from point C back to the standard PSB region B. The  $|\downarrow\uparrow\rangle$  state is not accessed during this measurement. (c) The two ESR peaks plotted as a function of detuning  $\epsilon$ . We use an incoherent ESR pulse of 100  $\mu\text{s}$  for this experiment. We identify the lower (higher) frequency peak corresponding to the QD1 (QD2) through the Stark-shift measurements reported in Supplementary Information. (d)-(f) Coherent spin control of QD2 showing (d), Rabi oscillations, (e), Rabi chevron, and (f), Ramsey fringes. We use frequency modulation technique to implement the ESR pulse scheme.  $\Delta f$  is the difference between the output and the carrier frequencies of the microwave source.

We have designed the orientation of the SET to maximize its sensitivity to inter-dot charge tunnelling events, and achieve good signal contrast for ST readout. As shown in the SET current histogram in Fig. 1(e), the signal peaks for standard PSB are separated by  $4.9\sigma$ , indicating a charge state readout fidelity  $> 99.8\%$ . The enhanced latching readout mechanism further increases the signal contrast between the singlet and triplet state, up to  $9.8\sigma$  (see Fig. 1(f),(g)). Such good contrast would allow charge readout with  $< 0.005\%$  error, however we find the latched meta state lifetime to be 2 ms or shorter. This is only one order of magnitude slower than the 120  $\mu\text{s}$  integration time that is required to achieve good signal separation for our experimental setup. Consequently, we notice a non-zero background between the singlet and triplet peaks in Fig. 1(g), evidencing decay from the triplet state to the singlet state during measurement. To avoid the spin readout error caused by the latched meta state relaxation as well as mapping errors [27], we chose the standard PSB region for readout. The triplet lifetime for standard PSB is 22 ms, which results in a  $\sim 0.5\%$  spin to charge conversion error. This reduces the total

fidelity of the single-shot ST readout using standard PSB to 99.3%. The latched metastate lifetime could be improved in future experiments by defining a third electron under G5 to fine-tune the electron tunnelling rate from QD1 and QD2 to the reservoir [28].

In this study, we control the spins of the electrons using an ac magnetic field generated by the on-chip microwave antenna [25]. In Fig. 2(a) we plot a schematic of the energy level diagram as a function of energy detuning  $\epsilon$  and in Fig. 2(b) the pulse sequences that we used to achieve ESR. As shown in Fig. 2(c) for  $B_z^0 = 150\text{ mT}$ , we find two resonance peaks that corresponds to rotations of QD1 (lower frequency) and QD2 (higher frequency). When we decrease  $\epsilon$ , the splitting between the two peaks increases, denoting the larger exchange coupling  $J$  between the electrons and mapping out the energy structure of the (1,3) - (0,4) anticrossing in the shallow detuning region. Next, we investigate the coherence of the spin qubits in low magnetic fields. By varying the ESR pulse time, we observe clear Rabi oscillations (Fig. 2(d)) at a magnetic field as low as  $B_z^0 = 150\text{ mT}$ , with  $T_2^{\text{Rabi}} = 18.6\ \mu\text{s}$ . In Fig. 2(e), we plot the Rabi chevron for one of the qubits at

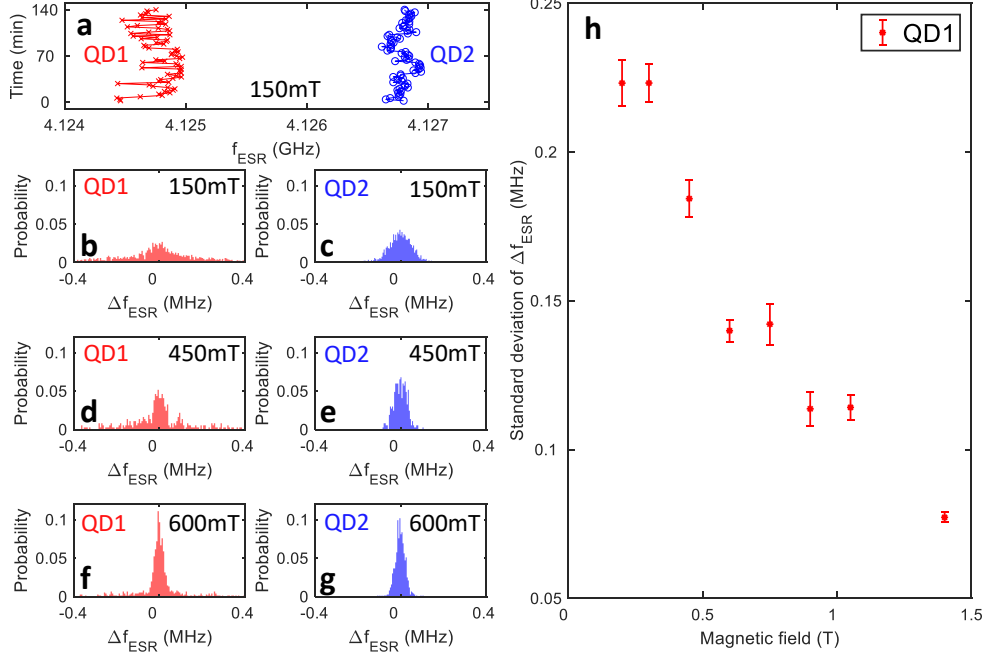


**Figure 3** |  $^{29}\text{Si}$ -induced ESR frequency fluctuation. (a) Measurement of ESR frequencies of the two qubits over a time period of 140 mins at 150 mT. There are significant fluctuations of the ESR frequencies of both qubits. Each point of measurement lasts about 2 mins. (b)-(g), Histograms of ESR frequency fluctuations for both qubits at various magnetic fields. The distribution becomes more concentrated at higher magnetic field. (h), Standard deviation of the fluctuation in ESR frequency of qubit QD1 plotted as a function of magnetic field. Each point is calculated based on a measurement that lasts 8 hours.

$B_z^0 = 450$  mT. We also use a Ramsey sequence (Fig. 2(f)) to measure  $T_2^*$  at various magnetic fields. The observed  $T_2^*$  values are reported in Tab. I.

The ability to perform coherent control on the spin states allows us to experimentally validate the combined initialization, control and measurement fidelity. We extract the maximum readout visibility for the  $|\uparrow\uparrow\rangle$  state by fitting the Rabi oscillations in Fig. 2(d). The maximum visibility is  $87.1 \pm 1.9\%$ , which is noticeably lower than our earlier estimate of the readout fidelity. During this measurement campaign, we observed frequent jumps in the ESR frequencies of both qubits due to spin flip of the surrounding nuclear of  $^{29}\text{Si}$ . This renders it difficult to keep the microwave frequency exactly on-resonance for the duration of the measurement (see also Fig. 2(e)). Therefore, the true readout visibility of the  $|\uparrow\uparrow\rangle$  state may not be reflected in this measurement. We also studied the maximum readout visibility for the three other spin states ( $|\downarrow\uparrow\rangle$ ,  $|\uparrow\downarrow\rangle$  and  $|\downarrow\downarrow\rangle$ ) using complementary measurements. The visibilities for  $|\downarrow\uparrow\rangle$  and  $|\uparrow\downarrow\rangle$  are as high as 99.3%, consistent with the readout fidelity estimated previously. The results are summarized in Tab. II with more details given in the Supplementary Information.

The robustness of ST readout allows us to employ tracking of the ESR frequency as a tool to study the nuclear spin environment of the spin qubits over a wide

range of magnetic fields from  $B_z^0 = 150$  mT to 1.4 T. As already noticeable in Fig. 2(e), we observe fluctuations of the ESR frequencies  $\Delta f_{\text{ESR}} = f_{\text{ESR}}(t_2) - f_{\text{ESR}}(t_1)$  of both qubits in time. More detailed data is shown in Fig. 3(a), where we track the ESR frequencies of both qubits over 140 mins. There is no correlation between  $\Delta f_{\text{ESR}}^{\text{QD1}}$  and  $\Delta f_{\text{ESR}}^{\text{QD2}}$ , indicating that any fluctuations are caused by a highly localized effect. We postulate the fluctuations in ESR frequency to be caused by the residual  $^{29}\text{Si}$  nuclear spins in the isotopically enriched substrate. Similar observations were already published in Ref. 7 on a different device. Figs. 3(b)-(g) show the histograms of  $\Delta f_{\text{ESR}}$  at three different magnetic fields for both qubits. We observe that the distribution of  $\Delta f_{\text{ESR}}$  becomes narrower as the magnetic field increases. To better quantify this effect, we plot the standard deviation of  $\Delta f_{\text{ESR}}^{\text{QD1}}$  as a function of magnetic field in Fig. 3(h). The standard deviation of  $\Delta f_{\text{ESR}}^{\text{QD1}}$  clearly decreases as the magnetic field increases. We believe the responsible mechanism is as follows: As the magnetic field reduces, the relative contribution of the hyperfine-mediated nuclear spin-spin interaction (whose coupling scales as the square of the hyperfine coupling constants over the electron Zeeman frequency) becomes larger relative to the field-independent dipole-dipole contribution in contributing to nuclear spin

diffusion, as previously observed and modelled for GaAs dots [29]. As this nuclear diffusion rate increases, a larger distribution of nuclear spins and therefore hyperfine shifts becomes accessible on the timescale of the experiment, broadening the observed distribution.

In summary, we have successfully operated spin qubits in a Si-MOS platform with a readout fidelity higher than 99.3 %. The ST readout scheme enables coherent control of single spins at a magnetic field of 150 mT and a resonance frequency as low as 4.1 GHz. This is a significant advantage for the scalability of Si-MOS qubit technology in building a quantum processor. In addition, our improved measurement has allowed the observation of important effects in magnetic noise occurring when Si-MOS qubits are operated in such a low magnetic field environment. Despite using an isotopically enriched  $^{28}\text{Si}$  substrate, there are still residual  $^{29}\text{Si}$  nuclear spins located in the vicinity of the qubits, causing fluctuations in the ESR frequencies. We observe the nuclear spin flip rate to decrease as the applied external magnetic field increases, an effect that may be reduced in future devices by reducing the  $^{29}\text{Si}$  isotopic content.

## METHODS

Figs. 1(a) and (b) show a scanning electron micrograph and a cross-sectional schematic of the sample used in this study. It is fabricated on top of a 900 nm thick, isotopically enriched  $^{28}\text{Si}$  epi-layer with 800 ppm residual  $^{29}\text{Si}$  on a natural silicon substrate [24]. We first grow a 7 nm thick thermal  $\text{SiO}_2$  plus a 3 nm atomic layer deposition (ALD) aluminium oxide to prevent gate to substrate leakage. Then, we use electron-beam lithography to write the nanoscale gate pattern and perform resist development in pre-cooled ( $-20^\circ\text{C}$ ) Methyl Isobutyl Ketone solution with ultrasound agitation. In the next step, we evaporate Pd onto the chip to form the gate electrodes. Since Pd has a much smaller grain size than aluminium, we routinely achieve gate features as narrow as 12 nm. A 2 nm thin Titanium (Ti) layer is evaporated prior to Pd deposition to enhance the cohesion of the Pd gate onto the oxide. The above lithography process is repeated several times to form the stack of Pd gate electrodes. Since Pd does not have a native oxide, we use ALD to grow 3-4 nm aluminium oxide on top of the gates to provide electrical insulation between different layers. Lastly, the sample is annealed in forming gas at  $400^\circ\text{C}$  for 15 mins to repair the damage caused by lithography.

Stanford Research Systems SIM928 modular programmable voltage sources are used to dc-bias all gate electrodes shown in Fig. 1(a) and (b). In addition, voltage pulses from an arbitrary waveform generator (Tektronix AWG7122) are applied to G1 and G3 through a voltage combiner. The bandwidth for dc bias (ac pulses) is 30 Hz (80 MHz). We use a nanoscale on-chip integrated 40-GHz antenna to generate the ac magnetic field to drive the electron spin resonance [25]. The antenna is powered by a vector microwave source (Agilent E8267D PSG). The sample is cooled down in an Oxford Instruments, liquid-helium cooled, dilution refrigerator with magnet. All measurements are performed at the phonon bath temperature of 37 mK.

## ACKNOWLEDGMENTS

We thank T. D. Ladd, A. Kiselev, W. Huang and A. Saraiva for enlightening discussions. We acknowledge support from the Australian Research Council (CE11E0001017 and CE170100039), the US Army Research Office (W911NF-13-1-0024 and W911NF-17-10198) and the NSW Node of the Australian National Fabrication Facility. The views and conclusions contained in this document are those of the authors and should not be interpreted as representing the official policies, either expressed or implied, of the Army Research Office or the U.S. Government. The U.S. Government is authorized to reproduce and distribute reprints for Government purposes notwithstanding any copyright notation herein. B.H. acknowledges support from the Netherlands Organization for Scientific Research (NWO) through a Rubicon Grant. K.M.I. acknowledges support from a Grant-in-Aid for Scientific Research by MEXT, NanoQuine, FIRST, and the JSPS Core-to-Core Program.

## AUTHOR INFORMATION

The authors declare no competing financial interests. Readers are welcome to comment on the online version of the paper. Correspondence and request for materials should be addressed to R.Z. (ruichen.zhao@unsw.edu.au) or A.S.D. (a.dzurak@unsw.edu.au).

- 
- [1] M. Veldhorst *et al.*, “An addressable quantum dot qubit with fault-tolerant control-fidelity,” *Nature Nanotechnology* **9**, 981 (2014).  
 [2] Erika Kawakami, P Scarlino, Daniel R Ward, FR Braakman, DE Savage, MG Lagally, Mark Friesen, Susan N Coppersmith, Mark A Eriksson, and LMK Vandersypen,

- “Electrical control of a long-lived spin qubit in a si/sige quantum dot,” *Nature nanotechnology* **9**, 666 (2014).  
 [3] Kenta Takeda, Jun Kamioka, Tomohiro Otsuka, Jun Yoneda, Takashi Nakajima, Matthieu R Delbecq, Shinichi Amaha, Giles Allison, Tetsuo Koderu, Shunri Oda, *et al.*, “A fault-tolerant addressable spin qubit

- in a natural silicon quantum dot,” *Science advances* **2**, e1600694 (2016).
- [4] TF Watson, SGJ Philips, Erika Kawakami, DR Ward, Pasquale Scarlino, Menno Veldhorst, DE Savage, MG Lagally, Mark Friesen, SN Coppersmith, *et al.*, “A programmable two-qubit quantum processor in silicon,” *Nature* **555**, 633 (2018).
- [5] D. M. Zajac *et al.*, “Resonantly driven cnot gate for electron spins,” *Science* **359**, 439–442 (2018).
- [6] J. Yoneda *et al.*, “A quantum-dot spin qubit with coherence limited by charge noise and fidelity higher than 99.9%,” *Nature nanotechnology* **13**, 102 (2018).
- [7] W. Huang *et al.*, “Fidelity benchmarks for two-qubit gates in silicon,” arXiv preprint arXiv:1805.05027 (2018).
- [8] C. H. Yang *et al.*, “Silicon qubit fidelities approaching stochastic noise limits via pulse optimisation,” arXiv preprint arXiv:1807.09500 (2018).
- [9] X Xue, TF Watson, J Helsen, DR Ward, DE Savage, MG Lagally, SN Coppersmith, MA Eriksson, S Wehner, and LMK Vandersypen, “Benchmarking gate fidelities in a si/sige two-qubit device,” arXiv preprint arXiv:1811.04002 (2018).
- [10] J. M. Elzerman *et al.*, “Single-shot read-out of an individual electron spin in a quantum dot,” *nature* **430**, 431 (2004).
- [11] M. Veldhorst, H. G. J. Eenink, C. H. Yang, and A. S. Dzurak, “Silicon cmos architecture for a spin-based quantum computer,” *Nature communications* **8**, 1766 (2017).
- [12] C. Jones *et al.*, “Logical qubit in a linear array of semiconductor quantum dots,” *Physical Review X* **8**, 021058 (2018).
- [13] T. A. Baart, M. Shafiei, T. Fujita, C Reichl, W. Wegscheider, and L. M. K. Vandersypen, “Single-spin ccd,” *Nature nanotechnology* **11**, 330 (2016).
- [14] Takafumi Fujita, Timothy Alexander Baart, Christian Reichl, Werner Wegscheider, and Lieven Mark Koenraad Vandersypen, “Coherent shuttle of electron-spin states,” *npj Quantum Information* **3**, 22 (2017).
- [15] M. A. Fogarty *et al.*, “Integrated silicon qubit platform with single-spin addressability, exchange control and single-shot singlet-triplet readout,” *Nature communications* **9**, 4370 (2018).
- [16] A. C. Johnson, J. R. Petta, C. M. Marcus, M. P. Hanson, and A. C. Gossard, “Singlet-triplet spin blockade and charge sensing in a few-electron double quantum dot,” *Phys. Rev. B* **72**, 165308 (2005).
- [17] A. West *et al.*, “Gate-based single-shot readout of spins in silicon,” arXiv preprint arXiv:1809.01864 (2018).
- [18] P Pakkiam *et al.*, “Single-shot single-gate rf spin readout in silicon,” arXiv preprint arXiv:1809.01802 (2018).
- [19] M. Urdampilleta *et al.*, “Gate-based high fidelity spin read-out in a cmos device,” arXiv preprint arXiv:1809.04584 (2018).
- [20] M Piore-Ladriere, T Obata, Y Tokura, Y-S Shin, Toshihiro Kubo, K Yoshida, T Taniyama, and S Tarucha, “Electrically driven single-electron spin resonance in a slanting zeeman field,” *Nature Physics* **4**, 776 (2008).
- [21] T. Ito *et al.*, “Four single-spin rabi oscillations in a quadruple quantum dot,” arXiv preprint arXiv:1805.06111 (2018).
- [22] A Crippa, R Ezzouch, A Aprá, A Amisse, L Houtin, B Bertrand, M Vinet, M Urdampilleta, T Meunier, M Sanquer, *et al.*, “Gate-reflectometry dispersive readout of a spin qubit in silicon,” arXiv preprint arXiv:1811.04414 (2018).
- [23] Brauns M., S. V. Amitonov, PC Spruijtenburg, and F. A. Zwanenburg, “Palladium gates for reproducible quantum dots in silicon,” *Scientific reports* **8**, 5690 (2018).
- [24] Kohei M. Itoh and Hideyuki Watanabe, “Isotope engineering of silicon and diamond for quantum computing and sensing applications,” *MRS Communications* **4**, 143157 (2014).
- [25] J. P. Dehollain, J. J. Pla, E. Siew, K. Y. Tan, A. S. Dzurak, and A. Morello, “Nanoscale broadband transmission lines for spin qubit control,” *Nanotechnology* **24**, 015202 (2012).
- [26] C. H. Yang, W. H. Lim, F. A. Zwanenburg, and A. S. Dzurak, “Dynamically controlled charge sensing of a few-electron silicon quantum dot,” *AIP Advances* **1**, 042111 (2011).
- [27] P. Harvey-Collard *et al.*, “High-fidelity single-shot readout for a spin qubit via an enhanced latching mechanism,” *Physical Review X* **8**, 021046 (2018).
- [28] T. Nakajima *et al.*, “Robust single-shot spin measurement with 99.5% fidelity in a quantum dot array,” *Physical review letters* **119**, 017701 (2017).
- [29] Łukasz Cywiński, Wayne M. Witzel, and S. Das Sarma, “Electron spin dephasing due to hyperfine interactions with a nuclear spin bath,” *Phys. Rev. Lett.* **102**, 057601 (2009).

$B_z^0$ (mT)	150	300	450
$f_{\text{Rabi}}$ (MHz)	0.25	0.25	0.33
$T_2^*$ ( $\mu\text{s}$ )	$1.4 \pm 0.21$	$2.5 \pm 0.3$	$3.3 \pm 0.65$

TABLE I | Observed  $T_2^*$  at three different magnetic fields  $B_z^0$  with its associated Rabi frequencies  $f_{\text{Rabi}}$ .

Spin state	Readout outcome	Visibility	Method	Limitation
$ \uparrow\uparrow\rangle$	Triplet	$87 \pm 1.9\%$	ESR driven $ \uparrow\uparrow\rangle \Leftrightarrow  \uparrow\downarrow\rangle$ oscillation	Control
$ \downarrow\uparrow\rangle$	Triplet	$99.3 \pm 2.3\%$	Exchange driven $ \downarrow\uparrow\rangle \Leftrightarrow  \uparrow\downarrow\rangle$ oscillation	Control
$ \uparrow\downarrow\rangle$	Singlet	$99.3 \pm 0.6\%$	$ \uparrow\downarrow\rangle \Rightarrow  \downarrow\downarrow\rangle$ $T_1$ relaxation	Thermalization
$ \downarrow\downarrow\rangle$	Triplet	$96.8 \pm 1.0\%$	$ \uparrow\downarrow\rangle \Rightarrow  \downarrow\downarrow\rangle$ $T_1$ relaxation	Thermalization

TABLE II | Maximum readout visibility for the four spin states of the two-qubit system. The error bar for  $|\uparrow\uparrow\rangle$  ( $|\downarrow\uparrow\rangle$ ) state visibility are derived from the fit of ESR (exchange) driven Rabi oscillations shown in Fig 2(d) (Fig. S2(c)). The exchange driven  $|\downarrow\uparrow\rangle \Leftrightarrow |\uparrow\downarrow\rangle$  oscillation experiment is reported in the Supplementary Information. The errors for  $|\uparrow\downarrow\rangle$  and  $|\downarrow\downarrow\rangle$  state visibility are derived from the fit of the exponential decay curve between the two states.